

# Sensitivity of Simulations of Double Detonation Type Ia Supernova to Integration Methodology

MICHAEL ZINGALE,<sup>1</sup> ZHI CHEN,<sup>1</sup> MELISSA RASMUSSEN,<sup>1</sup> ABIGAIL POLIN,<sup>2,3</sup> MAX KATZ,<sup>1</sup>  
ALEXANDER SMITH CLARK,<sup>1</sup> AND ERIC T. JOHNSON<sup>1</sup>

<sup>1</sup>*Department of Physics and Astronomy, Stony Brook University, Stony Brook, NY 11794-3800, USA*

<sup>2</sup>*The Observatories of the Carnegie Institution for Science, 813 Santa Barbara St., Pasadena, CA 91101, USA*

<sup>3</sup>*TAPIR, Walter Burke Institute for Theoretical Physics, 350-17, Caltech, Pasadena, CA 91125, USA*

## ABSTRACT

We study the coupling of hydrodynamics and reactions in simulations of the double detonation model for Type Ia supernovae. When assessing the convergence of simulations, the focus is usually on spatial resolution; however, the method of coupling the physics together as well as the tolerances used in integrating a reaction network also play an important role. In this paper, we explore how the choices made in both coupling and integrating the reaction portion of a simulation (operator / Strang splitting vs. the simplified spectral deferred corrections method we introduced previously) influences the accuracy, efficiency, and the nucleosynthesis of simulations of double detonations. We find no need to limit reaction rates or reduce the simulation timestep to the reaction timescale. The entire simulation methodology used here is GPU-accelerated and made freely available as part of the **Castro** simulation code.

*Keywords:* convection—hydrodynamics—methods: numerical

## 1. INTRODUCTION

Many different progenitor models for Type Ia supernovae (SNe Ia) are currently being explored to explain the observed spectroscopy diversity of SNe Ia explosions (Taubenberger 2017). One model, the double detonation model (Nomoto 1982; Woosley & Weaver 1984), involves a sub-Chandrasekhar mass white dwarf with an accreted He layer. A detonation in the He layer propagates around the star while sending a compression wave converging toward the center. This compression wave ignites a carbon detonation that then propagates outward from the center of the white dwarf, releasing enough nuclear binding energy to gravitationally unbind the star.

Many simulations have been performed on this model, varying the initial conditions, reaction network sizes, and resolution. Recent works show that, particularly in the case of a thin helium shell, a double detonation is viable progenitor for some SNe Ia (Fink et al. 2007; Moll & Woosley 2013; Shen & Bildsten 2014; Glasner et al. 2018; Shen et al. 2018; Polin et al. 2019; Townsley et al.

2019; Kushnir & Katz 2020; Gronow et al. 2020, 2021; Boos et al. 2021; Roy et al. 2022; Rivas et al. 2022). These works use slightly different methods of integrating the reaction network and controlling the timestep, which we discuss in the sections below. Our goal is to understand how sensitive a simulation of double detonations is to the details of how the reaction network is integrated and how it is coupled to hydrodynamics.

All of these works solve the compressible Euler equations with reactive and gravitational sources:

$$\frac{\partial \rho}{\partial t} + \nabla \cdot (\rho \mathbf{U}) = 0 \quad (1)$$

$$\frac{\partial(\rho \mathbf{U})}{\partial t} + \nabla \cdot (\rho \mathbf{U} \mathbf{U}) + \nabla p = \rho \mathbf{g} \quad (2)$$

$$\frac{\partial(\rho E)}{\partial t} + \nabla \cdot (\rho \mathbf{U} E + \mathbf{U} p) = \rho \mathbf{U} \cdot \mathbf{g} + \rho \dot{S} \quad (3)$$

$$\frac{\partial(\rho X_k)}{\partial t} + \nabla \cdot (\rho \mathbf{U} X_k) = \rho \dot{\omega}_k \quad (4)$$

where  $\rho$  is the mass density,  $\mathbf{U}$  is the velocity,  $E$  is the specific total energy,  $p$  is the pressure, and  $X_k$  are the mass fractions of the nuclei that react. The gravitational acceleration,  $\mathbf{g}$ , is obtained by solving the Poisson equation,

$$\nabla^2 \Phi = 4\pi G \rho, \quad (5)$$

(where  $G$  is Newton's constant) for the gravitational potential,  $\Phi$ , and defining  $\mathbf{g} = -\nabla \Phi$ . We note that  $\Phi$  is often approximated as a monopole or via a multipole expansion, which works well so long as the star stays reasonably spherically symmetric. The reaction network provides the species creation rate,  $\dot{\omega}_k$ , and the energy generation rate,  $\dot{S}$ . Finally, the system is closed via the equation of state:

$$p = p(\rho, e, X_k) \quad (6)$$

$$T = T(\rho, e, X_k) \quad (7)$$

where  $e$  is the specific internal energy, obtained as  $e = E - |\mathbf{U}|^2/2$ .

This is a multiphysics system of equations and the different physical processes have different associated timescales. Correspondingly, simulation codes use different methods to advance this system of equations. For hydrodynamics, explicit-in-time integration is usually used, with the timestep,  $\Delta t$ , restricted by the Courant limit (the precise form depends on whether we are doing unsplit hydrodynamics, dimensionally-split, or method of lines time-integration, see [Colella 1990](#)). In contrast, reactions are usually evolved using implicit-in-time integration, with many small steps taken to make up the hydrodynamics timestep  $\Delta t$ .

A key concern in modeling astrophysical reacting flows is the coupling of hydrodynamics and reactions. If a large amount of energy is dumped into a zone, then a large flow will result to carry away this energy, requiring tight communication between the reaction and hydrodynamics solvers. This coupling takes various forms in astrophysical simulation codes. The most common method is via operator splitting: the advection and reactive terms are treated independently, with each process working on the result of the other. Often, Strang-splitting ([Strang 1968](#)) is used, which alternates advection and reaction to yield second-order accuracy in time. The primary appeal of operator splitting is that it is easy to implement—the hydrodynamics and reaction solvers are largely independent of one another.

When using operator splitting, the density remains constant during the reactive update, since there is no reaction source in the mass continuity equation. The mass fractions,  $X_k$ , and energy evolve according to:

$$\frac{dX_k}{dt} = \dot{\omega}_k(\rho, T, X_k) \quad (8)$$

$$\frac{de}{dt} = \dot{S}(\rho, T, X_k) \quad (9)$$

$$T = T(\rho, e, X_k) \quad (10)$$

In the simplest approximation of operator splitting, the evolution of the mass fractions is solved alone, without integrating the temperature or energy, Eq. 9. This is the form that is used, e.g., in *Flash* (Fryxell et al. 2000, see also Townsley et al. 2016). A more accurate operator splitting also includes the energy evolution (perhaps in terms of temperature), solving the system Eqs. 8–10. This is the default in *Castro* (Almgren et al. 2010, 2020), and temperature evolution is also used in the works of Gronow et al. (2020, 2021) following the implementation of Pakmor et al. (2012). This evolution requires calling the equation of state each time we evaluate the right-hand side of the ODE system, potentially increasing the computational expense. However, as we showed in Zingale et al. (2021), this is needed to get second-order convergence. In our *AMReX-Astro Microphysics* library (AMReX-Astro Microphysics Development Team et al. 2023), we use C++ templating heavily to reduce the computational expense of the EOS calls by only computing the thermodynamic quantities needed by the integrator.

Detonations can be difficult to model numerically: the explosive energy released from reactions occurs on a much shorter timescale than the sound-crossing time of a zone. Many simulations use a simulation timestep based on the reaction timescale. For example, Fryxell et al. (1989) advocated for two constraints, one that limits the change in  $T$  over a timestep and another that limits the change of each mass fraction,  $X_k$  over a timestep. These can both be much more restrictive than the hydrodynamics timescale. Many current works instead use a reaction timestep based on the change in internal energy,  $e$ , over the timestep. This is an option in *Flash*. This energy-based reaction timestep limiter is used, for example, in the double detonation simulations of Kushnir & Katz (2020); Rivas et al. (2022). This helps keep the reactions and hydrodynamics coupled, but can greatly increase the expense of the simulation. It is also the case that since the timestep is so small,  $T$  does not change much over the simulation timestep, so evolving only the mass fractions may be reasonable. Artificially limiting the rates (Kushnir et al. 2013; Shen et al. 2018; Kushnir & Katz 2020; Boos et al. 2021) is also sometimes employed to prevent the reactions from releasing energy faster than the sound crossing timescale of a cell. Once the detonation ignition region is spatially resolved, this should not be needed. As we will see in the simulations presented here, if the reactions explicitly know about the advection that is taking place during the burn, neither of these limiting techniques appear to be needed.

In this paper, we focus on nucleosynthesis, exploring how reactions and hydrodynamics are coupled and the role of tolerances, the ignition of the second detonation, and the efficiency of the overall method. We also look at how the results behave with resolution. Finally, we discuss some of the difficulties encountered during the simulations.

## 2. SIMULATION SETUP

## 2.1. Numerical method

We use the freely-available **Castro** simulation code for all the simulations shown here. **Castro** solves the compressible Euler equations, Eqs. 1–4, using an unsplit PPM algorithm for advection (Colella 1990; Miller & Colella 2002; Colella & Woodward 1984), with the Riemann solver from Colella & Glaz (1985) and the general stellar equation of state of Timmes & Swesty (2000). **Castro** also advects internal energy together with total energy, in the dual-energy formalism introduced in Bryan et al. (1995) (see Katz et al. 2016 for details on the implementation). In all simulations, the CFL constraint is the only timestep constraint used. Self-gravity is done using a full Poisson solve using geometric multigrid, with Dirichlet boundary conditions on the domain boundary computed via a multipole expansion with a maximum order of 6. **Castro** uses adaptive mesh refinement (AMR) via the AMReX library (Zhang et al. 2019), with subcycling throughout the AMR hierarchy, so finer grids are advanced at a smaller timestep than the coarse grids.

In Zingale et al. (2022), we introduced a method based on the ideas of spectral deferred corrections (Dutt et al. 2000; Bourlioux et al. 2003) for coupling reactions and hydrodynamics. We termed the method “simplified-SDC.” In the simplified-SDC method, the overall time-integration is done iteratively, with the hydrodynamics seeing an explicit reactive source and the reaction update evolving an ODE system that includes a piecewise-constant-in-time advective source,  $[\mathcal{A}(\mathbf{u})]^{n+1/2}$ ,

$$\frac{\partial \mathbf{u}}{\partial t} = \mathbf{R}(\mathbf{u}) + [\mathcal{A}(\mathbf{u})]^{n+1/2} \quad (11)$$

Here,  $\mathbf{u}$  is the conserved state,  $\mathbf{u} = (\rho, \rho \mathbf{U}, \rho E, \rho X_k)^\top$ ,  $\mathbf{R}(\mathbf{u})$  are the reactive sources, and  $[\mathcal{A}(\mathbf{u})]^{n+1/2}$  is an approximation to the advective update over the timestep, as computed by the corner transport upwind formulation of the piecewise parabolic method. Crucially, this advective term includes an explicit reaction source term and, likewise, the reaction update, Eq. 11, means that the reactions will “see” what advection is doing as the reaction network is integrated.

The reaction system is integrated using a version of the VODE ODE integrator (Brown et al. 1989) ported to C++. Our modifications to this integrator are described in Zingale et al. (2022). We use an analytic approximation to the Jacobian (the main approximation is that the species derivatives of the screening function are not included) and found that we get the best results when we disable the caching of the Jacobian in the integrator.

In addition to the time-integration strategy, integrating the reaction ODE system requires specifying tolerances, usually both an absolute,  $\epsilon_{\text{abs}}$ , and relative tolerance,  $\epsilon_{\text{rel}}$ , that are combined together into a weight of the form:

$$w_i = \epsilon_{\text{abs},i} + \epsilon_{\text{rel},i} |y_i| \quad (12)$$

where the  $y_i$  is one of the variables being integrated by the ODE integrator and  $i$  its the index, indicating that different tolerances can be used for each variable. Traditionally one set of tolerances is used for the mass fractions and another for the energy (if it is integrated). We will refer to the species tolerances as  $\epsilon_{\text{abs}}(X_k)$  and  $\epsilon_{\text{ref}}(X_k)$  and the energy tolerances as  $\epsilon_{\text{abs}}(e)$  and  $\epsilon_{\text{rel}}(e)$ . Unfortunately, the tolerances used by simulations are not normally reported in papers, and in many cases, may not be easily controlled by a code user at runtime. Some examples can be found in publicly available networks. For example, the freely available version of the **aprox13** network uses  $\epsilon_{\text{rel}} = 10^{-5}$  and a floor on the mass fractions corresponding to  $\epsilon_{\text{abs}} = 10^{-6}$ . We caution that different integrators may use different error measures or norms so comparing the tolerance values across integrators can be

difficult. Since the simplified-SDC update works in terms of the conserved variables,  $\mathcal{U}$ , we apply a density weighting to the absolute tolerances when comparing to the values used in Strang integration (see Zingale et al. 2022).

All simulations use the same reaction network: the `subch_simple` as described in Chen et al. (2023). This includes 22 nuclei and 94 rates from ReacLib (Cyburt et al. 2010) and is produced with `pynucastro` (Smith et al. 2023). Importantly, we include  $^{14}\text{N}(\alpha, \gamma)^{18}\text{F}(\alpha, p)^{21}\text{Ne}$  which creates protons to allow for  $^{12}\text{C}(p, \gamma)^{13}\text{N}(\alpha, p)^{16}\text{O}$ . This sequence can be faster than  $^{12}\text{C}(\alpha, \gamma)^{16}\text{O}$ , as pointed out by Shen & Bildsten (2009) and is important for getting the detonation speed correct. To reduce the size of the network, we have `pynucastro` combine some  $(\alpha, p)(p, \gamma)$  and  $(\alpha, \gamma)$  rates into an effective  $(\alpha, \gamma)$  rate. We also approximate the neutron captures for  $^{12}\text{C}(^{12}\text{C}, n)^{23}\text{Mg}(n, \gamma)^{24}\text{Mg}$ ,  $^{16}\text{O}(^{12}\text{C}, n)^{31}\text{S}(n, \gamma)^{32}\text{S}$ ,  $^{16}\text{O}(^{16}\text{O}, n)^{31}\text{S}(n, \gamma)^{32}\text{S}$ , eliminating the intermediate nucleus in each sequence. Together these approximations make the 22 nuclei network approximate a 31 nuclei network. Screening is provided following the procedure in Wallace et al. (1982), combining the screening functions of Graboske et al. (1973); Alastuey & Jancovici (1978); Itoh et al. (1979).

Our choice of reaction network size falls in the middle of those reported in the literature. Townsley et al. (2019); Boos et al. (2021) use a 55-isotope network, but do not describe whether energy / temperature is integrated together with the rates (although, based on Townsley et al. 2016 it likely is not). Gronow et al. (2020, 2021) use more than 30 isotopes, and use the integration method from Pakmor et al. (2012). Rivas et al. (2022) use the 13-isotope `aprox13` network, and likewise do not state whether energy / temperature is integrated together with the rates, although `Flash` does not usually include energy/temperature evolution with the reactions. Moll & Woosley (2013) used the `aprox19` network together with a table from a large network to better describe the nucleosynthesis. While they used `Castro`, the temperature evolution during the reactions was simpler than in the current versions of `Castro`. Roy et al. (2022) also use `aprox19`. The `aprox13` and `aprox19` networks do not have the reaction sequences discussed in Shen & Bildsten (2009) and will lead to an underestimate of the He detonation speed, which in turn affects where the compression ignites the C detonation. None of these works discuss the integration tolerances. Several works also disable burning in shocks (this includes Kushnir & Katz 2020; Gronow et al. 2020, 2021; Rivas et al. 2022 and likely others as this can be the default behavior in some codes). We do not take that approach here in part because the burning will explicitly see what is happening from advection as we integrate the network (see also Papatheodore & Messer 2014).

If during the advance of a timestep an error is generated (negative density, ODE integration fails because it cannot meet the tolerances required or takes too many steps, mass fractions don't sum to 1, CFL constraint violated at the new time), the step is thrown-out and retried with a smaller timestep. This is done on a level-by-level basis in the overall AMR subcycling hierarchy. This is discussed further in Zingale et al. (2022).

## 2.2. Initial model

We considered an extreme version of the double detonation scenario in Zingale et al. (2022)—a very large perturbation was applied to drive a detonation directly in a pure carbon white dwarf. We showed that the Strang-splitting integration method (including energy evolution) had difficulty with the integration unless we used tighter tolerances, while the simplified-SDC method was well-behaved. Here we look at a much more realistic setup for a double detonation and look at convergence with integration method and resolution. Our new model uses a much smaller perturbation that drives a

He detonation around the C/O white dwarf and a compression wave that results in the ignition of a C detonation near the center of the star.

We will run a suite of simulations all using the same initial model, constructed following the methodology in [Zingale et al. \(2013\)](#). We use an isothermal core of C/O of  $1.1 M_{\odot}$  with  $T = 10^7$  K and a thin transition region where the temperature ramps up to  $1.75 \times 10^8$  K and the composition changes to 99%  $^4\text{He}$  and 1%  $^{14}\text{N}$ . This He envelope is then integrated isentropically. The density of the transition from the underlying CO white dwarf to the He envelope was selected to yield an envelope mass of  $0.05 M_{\odot}$ . The code for generating the model is freely available ([AMReX-Astro initial\\_models team et al. 2023](#)). Our choice of white dwarf mass and envelope mass was inspired by our previous work on modeling the convective runaway in double detonations ([Jacobs et al. 2016](#)), where we found larger envelopes and/or core masses are needed to get the localized runaway that could lead to a double detonation.

We place a small temperature perturbation in the He layer using the same form as in [Zingale et al. \(2022\)](#):

$$T = T_0 \{1 + X(^4\text{He})f [1 + \tanh(2 - \sigma)]\} \quad (13)$$

where

$$\sigma = [x^2 + (y - R_0)^2]^{1/2} / \lambda \quad (14)$$

and

$$R_0 = R_{\text{pert}} + R_{\text{base}} \quad (15)$$

where,  $R_{\text{base}}$  is the radius at which the helium layer begins (determined as the radius where  $X(^4\text{He})$  first goes beyond 0.5) and  $R_{\text{pert}}$  is the distance above the base to put the perturbation. We choose  $R_{\text{pert}} = 100$  km. The temperature is perturbed above the initial model value, denoted as  $T_0$  here. The amplitude of the perturbation is  $f = 3$  and the scale of the perturbation is  $\lambda = 12.5$  km. This is a very small perturbation, with a peak temperature of about  $1.1 \times 10^9$  K, spread over roughly 2 zones (in our references 20 km resolution simulations). This is large enough to seed the initial He detonation in the envelope.

### 2.3. Suite of Runs

All simulations use a 2D axisymmetric geometry with a size of  $5.12 \times 10^9$  cm by  $1.024 \times 10^{10}$  cm. This is much larger than the initial size of the star, giving it plenty of room to expand (we note that the figures shown in the results section are all zoomed in on the star). AMR is used, with a coarse grid of  $640 \times 1280$  zones. For most simulations, 2 levels of refinement are used (each a jump of  $2\times$ ) giving a maximum resolution of 20 km. The refinement strategy is picked to refine the star and any regions where the temperature is greater than  $10^8$  K. For the low-density regions outside of the star, we use a sponge term on the momentum equation to prevent the very low-density material that is not in hydrostatic equilibrium from raining down on the star (see [Eiden et al. 2020](#) for a discussion of the sponge term in **Castro**).

Our base simulation, which we refer to as SDC-0.2, uses the simplified-SDC integration, a CFL number of 0.2, and sets  $\epsilon_{\text{rel}} = \epsilon_{\text{abs}} = 10^{-5}$  for both the species and energy. Overall, the simulation requires 21,784 coarse grid timesteps to evolve to 1.0 s of simulation time. Table 1 summarizes the suite of different simulations we consider. We also show the total amount of  $^{56}\text{Ni}$  produced at 1.0 s of simulation time for each simulation.



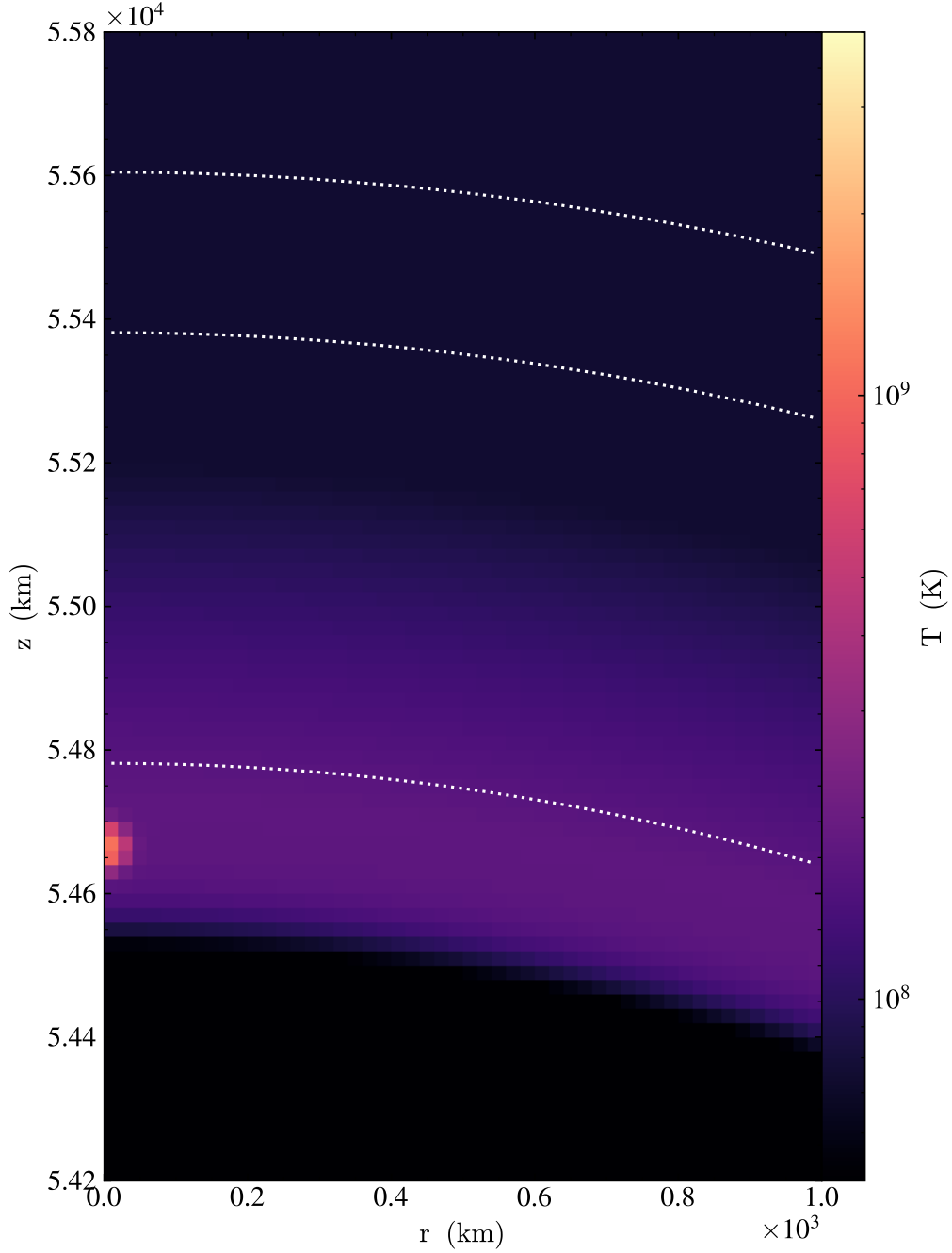


**Figure 1.** Zoom-in on the initial hotspot 100 km above the He-C interface. The dotted contours show densities of  $10^4$ ,  $10^5$ , and  $10^6$  g cm $^{-3}$

The simulations are all run on the OLCF Frontier machine, using 4 nodes / 32 AMD GPUs. The data is moved to the GPUs at the start of the simulation and all computation is done there. Our GPU offloading strategy (Katz et al. 2020) takes advantage of the AMReX C++ parallel-for abstraction

**Table 1.** Parameters for our simulation suite.

name	coupling	CFL	fine grid res	$\epsilon_{\text{atol}}(X_k)$	$\epsilon_{\text{rtol}}(X_k)$	$\epsilon_{\text{atol}}(e)$	$\epsilon_{\text{rtol}}(e)$	$M_{56\text{Ni}}(t = 1.0 \text{ s})/M_{\odot}$
SDC-0.2	simplified-SDC	0.2	20 km	$10^{-5}$	$10^{-5}$	$10^{-5}$	$10^{-5}$	0.652
SDC-0.4	simplified-SDC	0.4	20 km	$10^{-5}$	$10^{-5}$	$10^{-5}$	$10^{-5}$	0.654
Strang-0.2	Strang	0.2	20 km	$10^{-5}$	$10^{-5}$	$10^{-5}$	$10^{-5}$	0.734
Strang-0.05	Strang	0.05	20 km	$10^{-5}$	$10^{-5}$	$10^{-5}$	$10^{-5}$	0.747
Strang-tol	Strang	0.2	20 km	$10^{-8}$	$10^{-5}$	$10^{-5}$	$10^{-5}$	0.665
SDC-40km	simplified-SDC	0.2	40 km	$10^{-5}$	$10^{-5}$	$10^{-5}$	$10^{-5}$	0.647
SDC-10km	simplified-SDC	0.2	10 km	$10^{-5}$	$10^{-5}$	$10^{-5}$	$10^{-5}$	0.652
SDC-5km	simplified-SDC	0.2	5 km	$10^{-5}$	$10^{-5}$	$10^{-5}$	$10^{-5}$	0.652

layer to be performance portable. All of the simulation code is on GitHub<sup>1</sup> and the inputs files, global diagnostics used to make the line plots shown below, and metadata describing the git hashes, compiler environment, and runtime parameters for all of the simulations is available on Zenodo at Zingale et al. (2023).

### 3. RESULTS

Figure 2 shows the evolution of the temperature field for the base simulation. The initial perturbation is placed at the north pole at  $t = 0$  and leads to a detonation in the He layer that begins to wrap around the star. By 0.1 s the detonation is almost halfway around the star and by 0.2 s is almost at the south pole. Figure 3 shows a Schlieren-style plot, which highlights density gradients (see, e.g., Svakhine et al. 2005 a discussion of this type of visualization). We plot  $\log_{10}(|\rho^{-1}\nabla^2\rho|)$ —this clearly shows a compression wave launched by the early evolution of the He detonation propagating inward toward the center of the white dwarf.

Between  $t = 0.3$  and  $t = 0.7$  s the burning is confined to the outer layer, but the compression wave continues to advance inward, converging slightly off-center at around  $t = 0.7$  s. This highlights how the speed of the He detonation is important in determining how off-center the C detonation ignition will be. A faster He detonation means the convergence happens at higher density, making the C ignition easier. Our choice of network was motivated by ensuring that we capture the energy release from He burning accurately, in particular the inclusion of the  $^{12}\text{C}(p, \gamma)^{13}\text{N}(\alpha, p)^{16}\text{O}$  sequence.

In the bottom row of Figure 2, we see the second detonation ignites near the center of the star and begin to propagate outward. By 1.0 s, it has evolved past the initial radius of the star and into the extended ash layer left behind by the previous He detonation.

#### 3.1. Time-integration and Nucleosynthesis

We now look at the details of the nucleosynthesis and how Strang integration compares to our base simplified-SDC simulation. We will focus on the case where the energy equation is integrated together with the species while doing Strang-splitting. For the Strang comparisons, we will vary the CFL number and the integration tolerances. We note that we were not able to run the case

<sup>1</sup> <https://github.com/amrex-astro/>



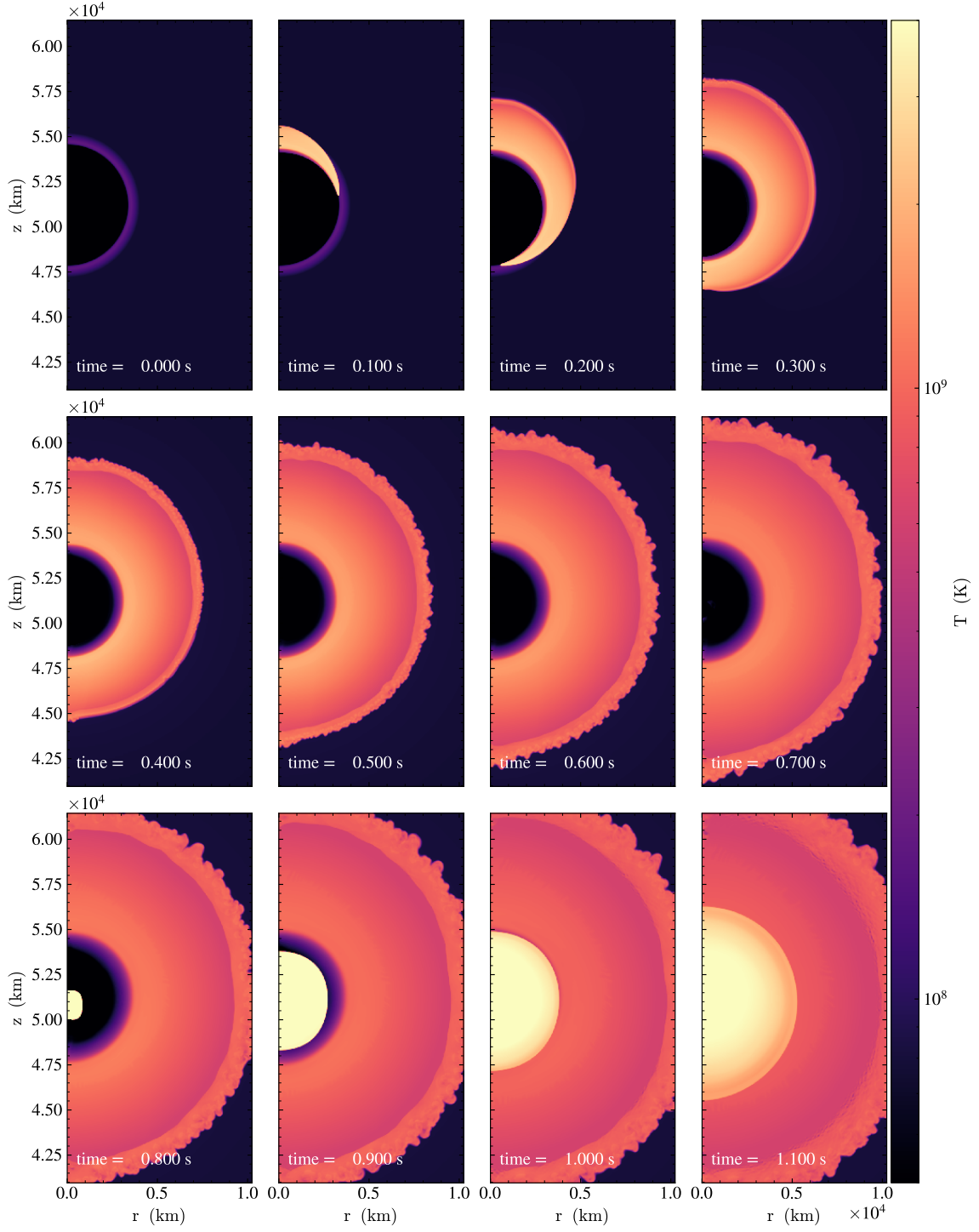


**Figure 2.** Time-sequence of the SDC run showing the temperature.

where the temperature is held fixed during the Strang burn past the C detonation ignition (for the CFL numbers we consider) without the integrator encountering problems (as we note below, the temperature became unphysically high). This is likely why many works taking this approach use a reaction-based timestep.

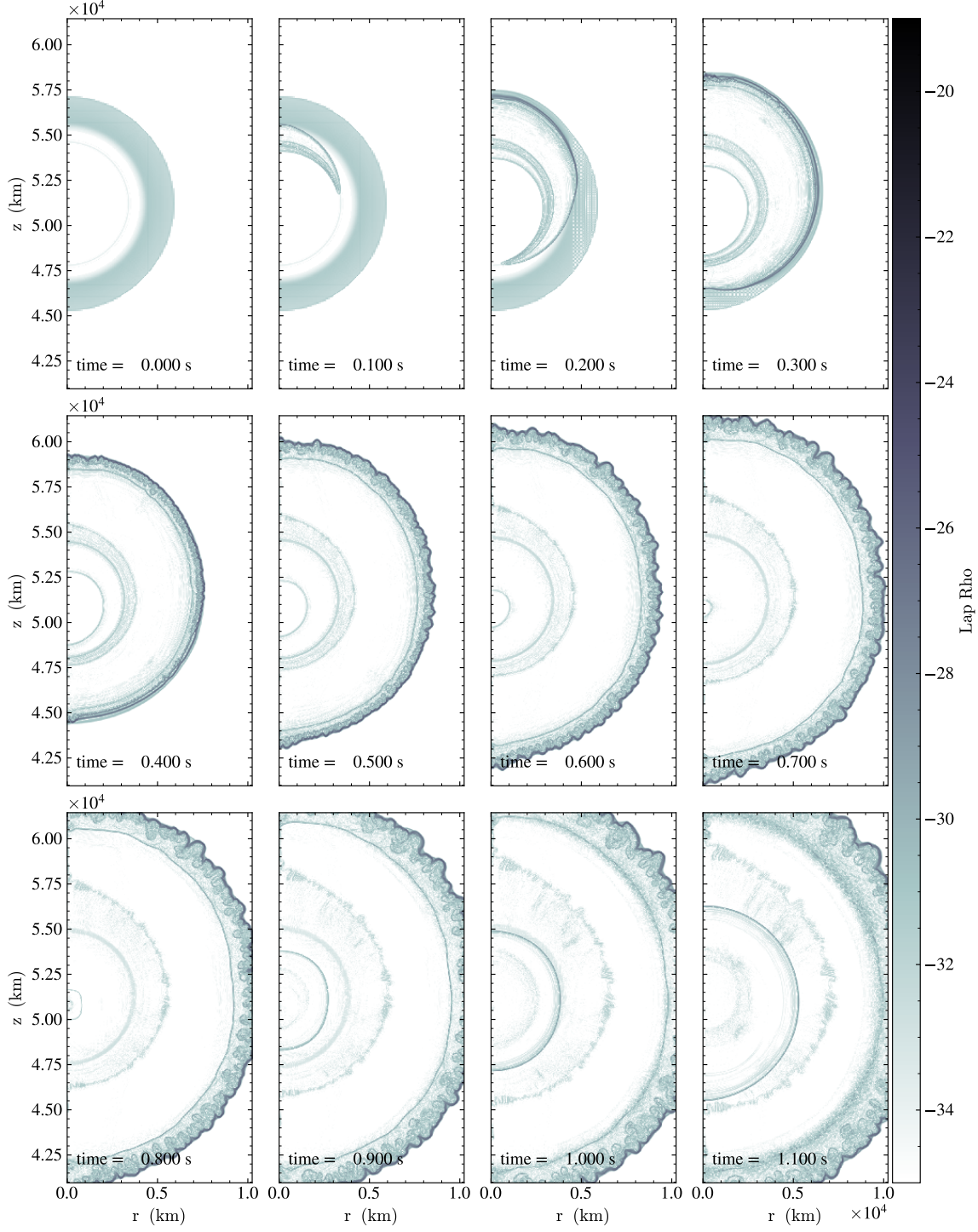


**Figure 3.** Time-sequence of the SDC run showing the compression.

Figure 4 shows the total amount of  $^{56}\text{Ni}$  as a function of time for the suite of simulations. The black solid line is for our SDC-0.2 simulation discussed above. The general trend we see is that the  $^{56}\text{Ni}$  mass increases quickly until 0.2 s, corresponding to the timescale for the He detonation to wrap around the star. About  $0.02M_{\odot}$  of  $^{56}\text{Ni}$  is produced during this phase. Around 0.7 s, we see the  $^{56}\text{Ni}$

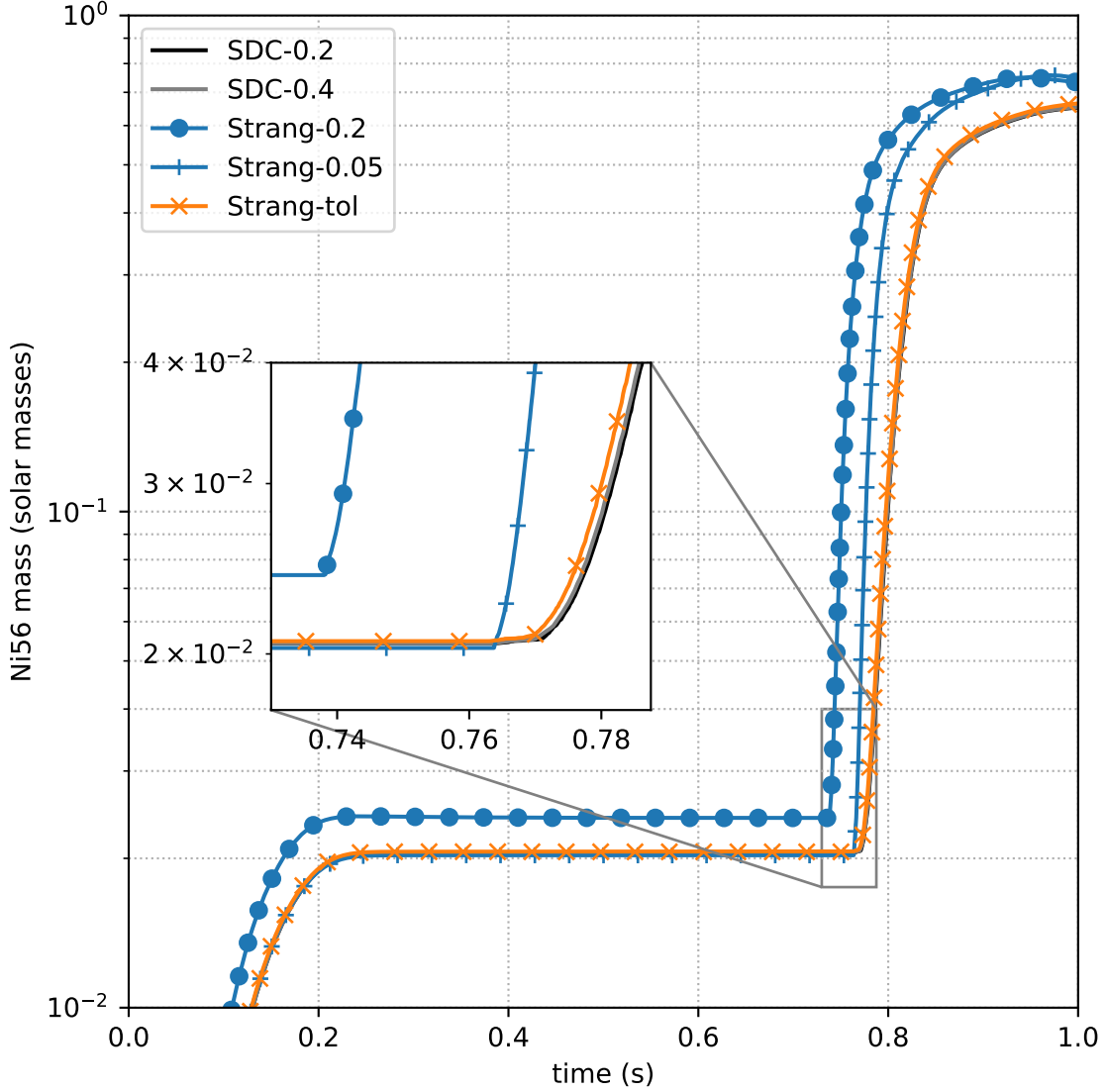


**Figure 4.**  $^{56}\text{Ni}$  mass vs. time for the different simulations.

mass steeply increase, corresponding to the ignition of the C detonation and then level off at 1.0 s, corresponding to the detonation making it through the entire star. We tabulate the  $^{56}\text{Ni}$  mass in Table 1 at 1.0 s as well.

The blue curves on Figure 4 show the Strang runs with the same default integrator tolerances, but one with CFL = 0.2 (Strang-0.2) and the other with CFL = 0.05 (Strang-0.05). We see both of them over-produce  $^{56}\text{Ni}$  at the end, but the smaller CFL run agrees with the amount of  $^{56}\text{Ni}$  produced during the He det phase. Both lead to an earlier ignition of the C detonation.

The orange curve on Figure 4 shows the Strang runs with the CFL = 0.2, but now different integrator tolerances. The tolerances for energy, unchanged:  $\epsilon_{\text{abs}}(e) = \epsilon_{\text{rel}}(e) = 10^{-5}$ , but now the simulation labeled Strang-tol uses  $\epsilon_{\text{abs}}(X_k) = 10^{-8}$  and  $\epsilon_{\text{rel}}(X_k) = 10^{-5}$ , allowing it to track lower abundances of trace species. We see that Strang-tol matches the SDC-0.2 calculation well—the curves are nearly

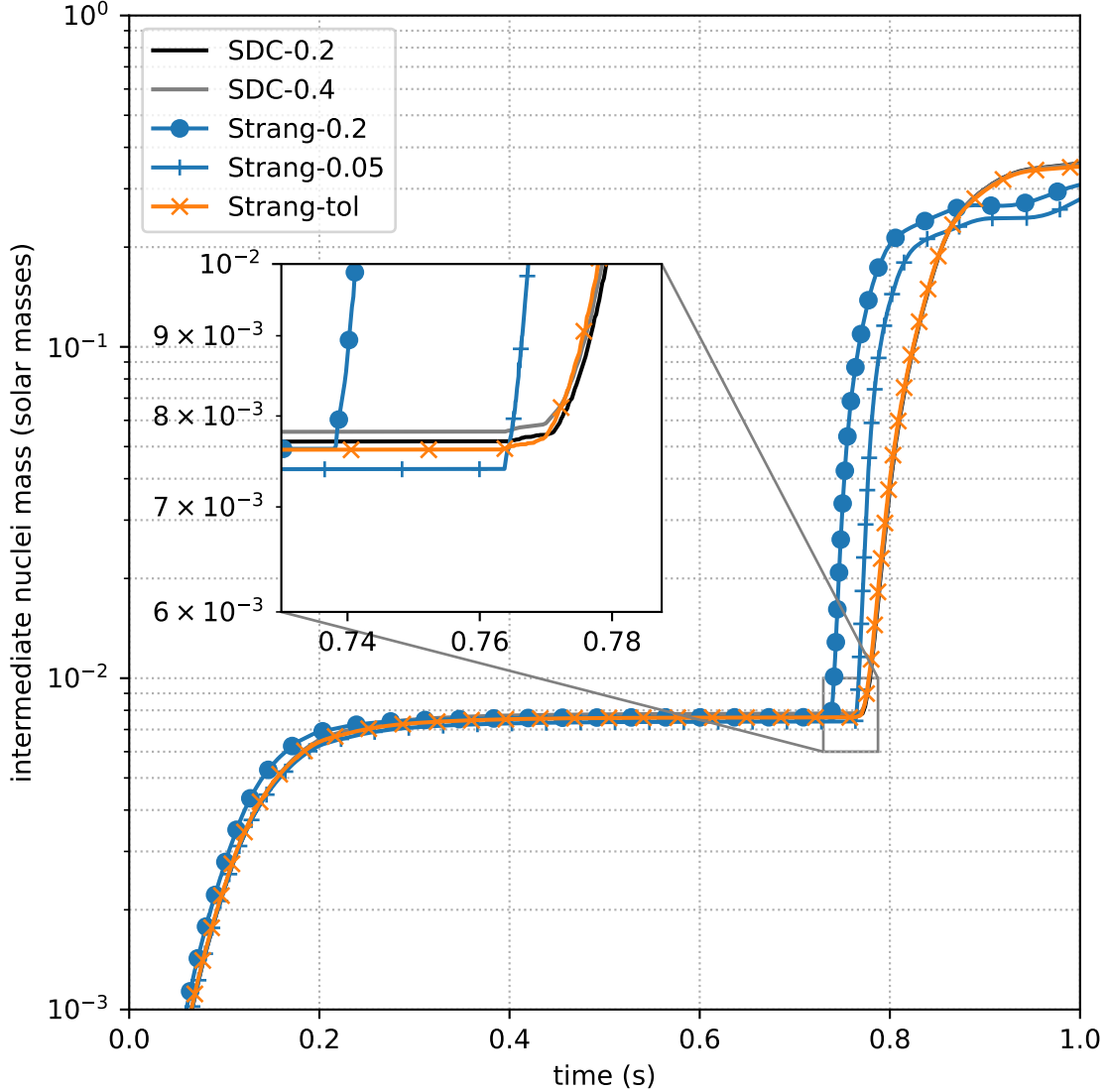


**Figure 5.** Total mass of the the nuclei from  $^{28}\text{Si}$  to  $^{44}\text{Ti}$  vs. time for the different simulations.

on top of one another. This agrees with what we observed with the more extreme model considered in Zingale et al. (2022), and gives us confidence that the simplified-SDC method works well.

Figure 5 shows the total mass of the nuclei from  $^{28}\text{Si}$  to  $^{44}\text{Ti}$  vs. time. We see the same general trend as with the  $^{56}\text{Ni}$  plot, with the Strang-tol run agreeing with the SDC runs. However, in this case, Strang-0.2 and Strang-0.05 underproduce these elements after the C detonation is established.

Figure 6 shows the peak temperature vs. time. From the initial hotspot, we see a quick increase to  $\sim 3.3 \times 10^9$  K as the He detonation propagates around the star. The peak temperature then begins to drop as the main burning in the He layer is over. After 0.75 s there is a sharp increase in the temperature to over  $7 \times 10^9$  K—this is the ignition of the central C detonation. We note that at this extremely high temperature, the nuclei are almost certainly in nuclear statistical equilibrium (NSE), so replacing the burning with an NSE solver would make the simulations more efficient (as done, e.g., in Ma et al. 2013; Kushnir & Katz 2020). This will be explored in the future. It is also interesting to

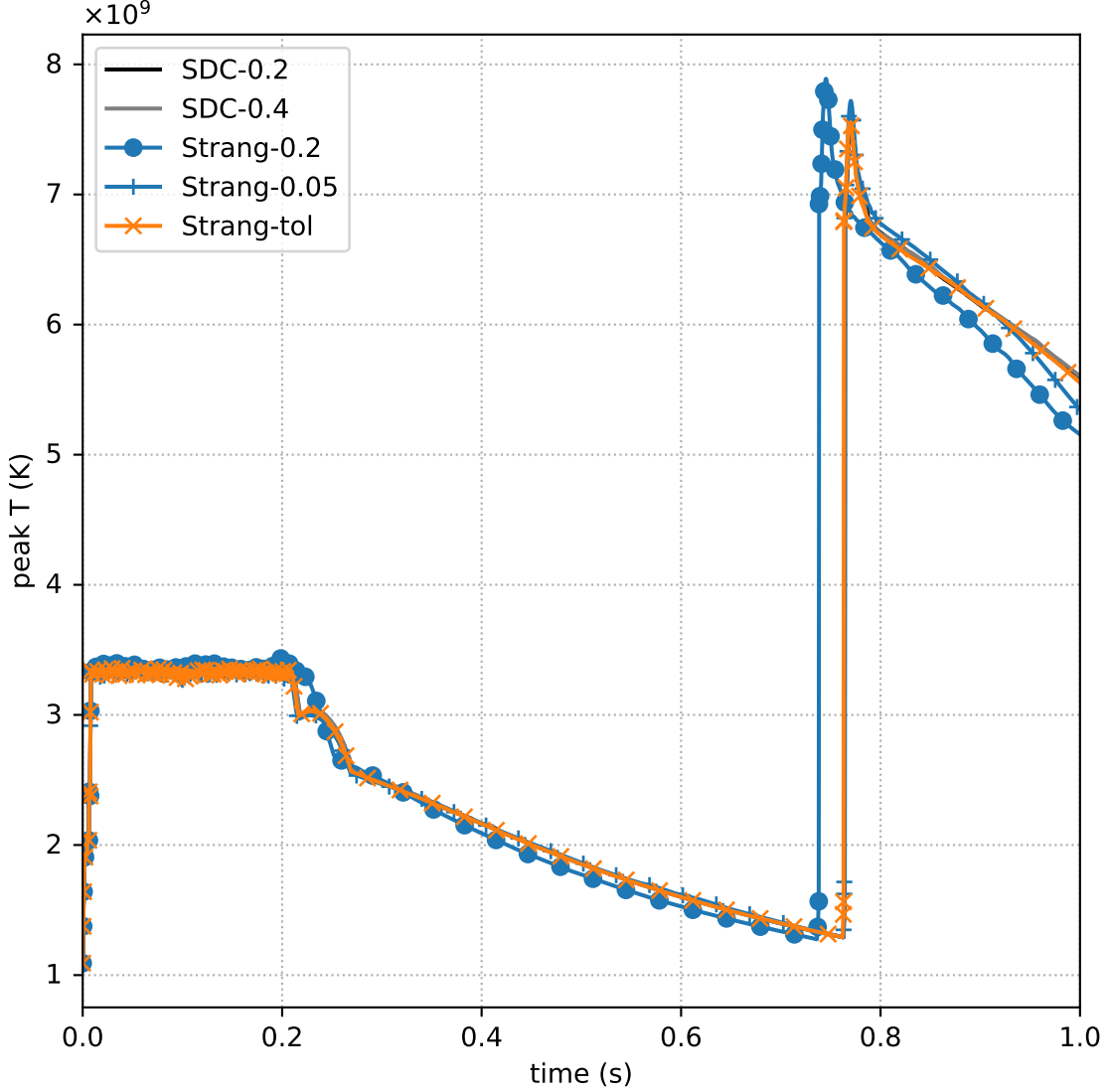


**Figure 6.** Peak temperature vs. time for the different simulations.

note here that the Strang-0.05 run agrees with the temperature curve for the SDC runs, so reducing the CFL number with Strang coupling does bring the temperature under control. We also note that if we try to use Strang coupling without any  $T$  or energy evolution, the peak temperature reaches  $1.2 \times 10^{10}$  K during the C detonation ignition, and we are unable to run further (the ODE integrator encounters problems).

Finally, we consider what happens if we use a longer timestep with the simplified-SDC algorithm. SDC-0.4 uses a CFL number of 0.4, and the  $^{56}\text{Ni}$  mass is shown as the gray line in Figure 4. As we see, it is virtually on top of the line corresponding to SDC-0.2, demonstrating that we remain converged when taking a larger timestep. We note however, that the ODE integrator does have a harder time evolving the coupled system when the C detonation ignites (usually isolated to just a few zones each timestep). As a result, at the point of the C detonation ignition, we switched the integrator to using a difference-approximation to the Jacobian (Radhakrishnan & Hindmarsh 1993) instead of the

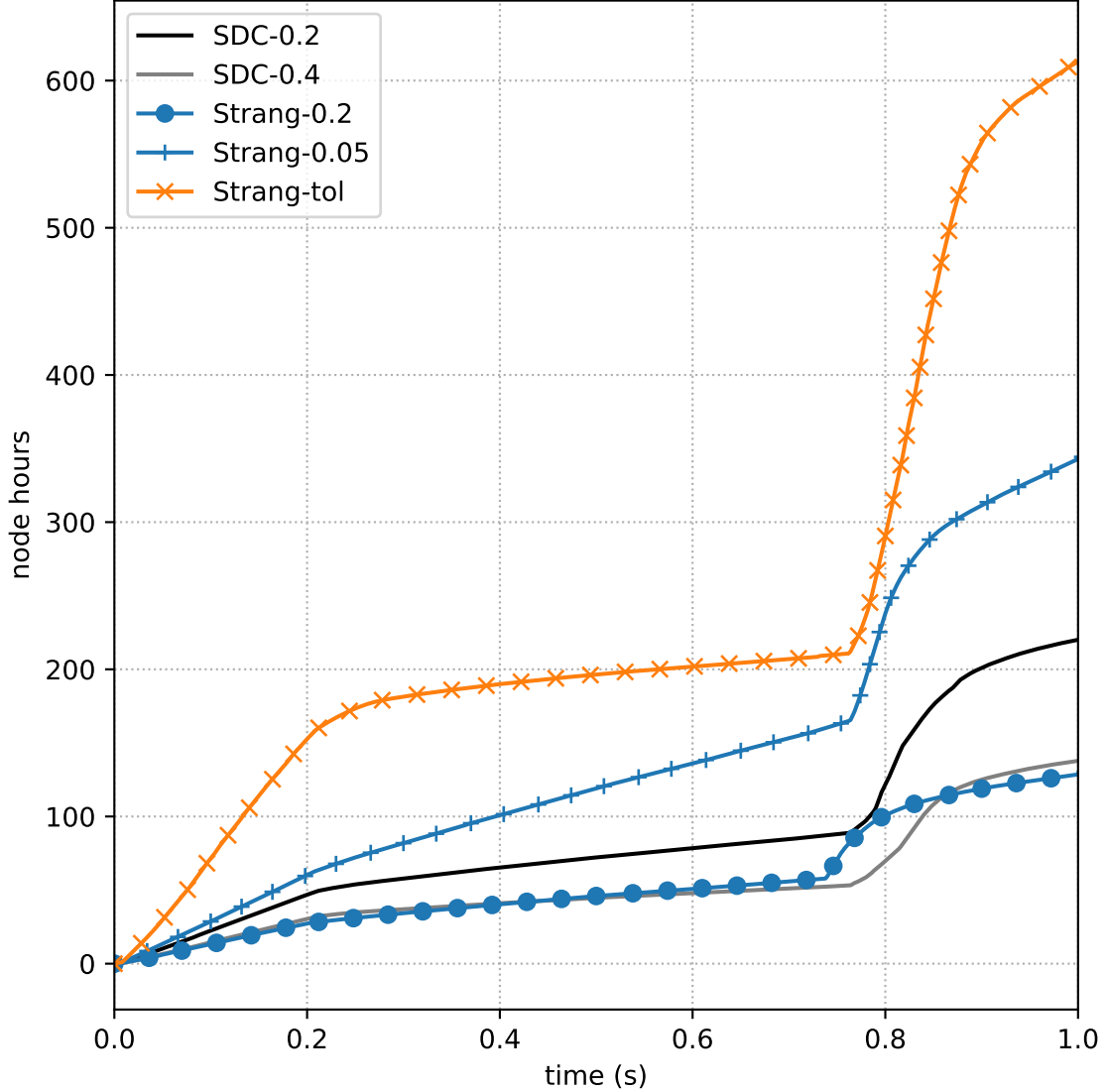


**Figure 7.** node hours of GPU time for the different simulations.

analytic Jacobian, and the simulation ran without difficulties afterwards. This highlights however that the integrator does work hard at times, and suggests a focus on exploring different integrators or techniques to improve the robustness of the ODE integration.

### 3.2. Computational Efficiency

We next want to ask whether the simplified-SDC method is more expensive. Figure 7 shows the computational expense of the simulations, in terms of node hours. All simulations were run on 4 nodes (32 AMD GPUs total). We note that we have not spent much time on optimizing the load-balancing of these simulations, so we should consider this to be only a guide. AMReX divides the domain up into boxes at each level. On a level, these boxes can vary in size, but all have the same resolution. We require each box to be a multiple of 32 zones on a side, with a maximum length in a dimension of 256 zones. At the start of the simulation, there are 56 boxes on the finest level



(representing 0.77% of the domain) and at 1 s of evolution, there are 60 boxes covering 5.64% of the domain. The figure shows that the Strang-0.2 simulation is the cheapest, but as we saw above, this does not get the nucleosynthesis correct. All of the other Strang simulations are more costly than the baseline SDC simulation. In particular, the Strang run with the tightest tolerances, Strang-tol, that agreed with the  $^{56}\text{Ni}$  produced by SDC-0.2 is about  $3\times$  more costly. As we also see, the SDC-0.4 simulation runs very quickly—about as fast as the Strang-0.2 simulation. This shows that not only does the simplified-SDC simulation accurately evolve the nucleosynthesis, it does so in a very efficient fashion.

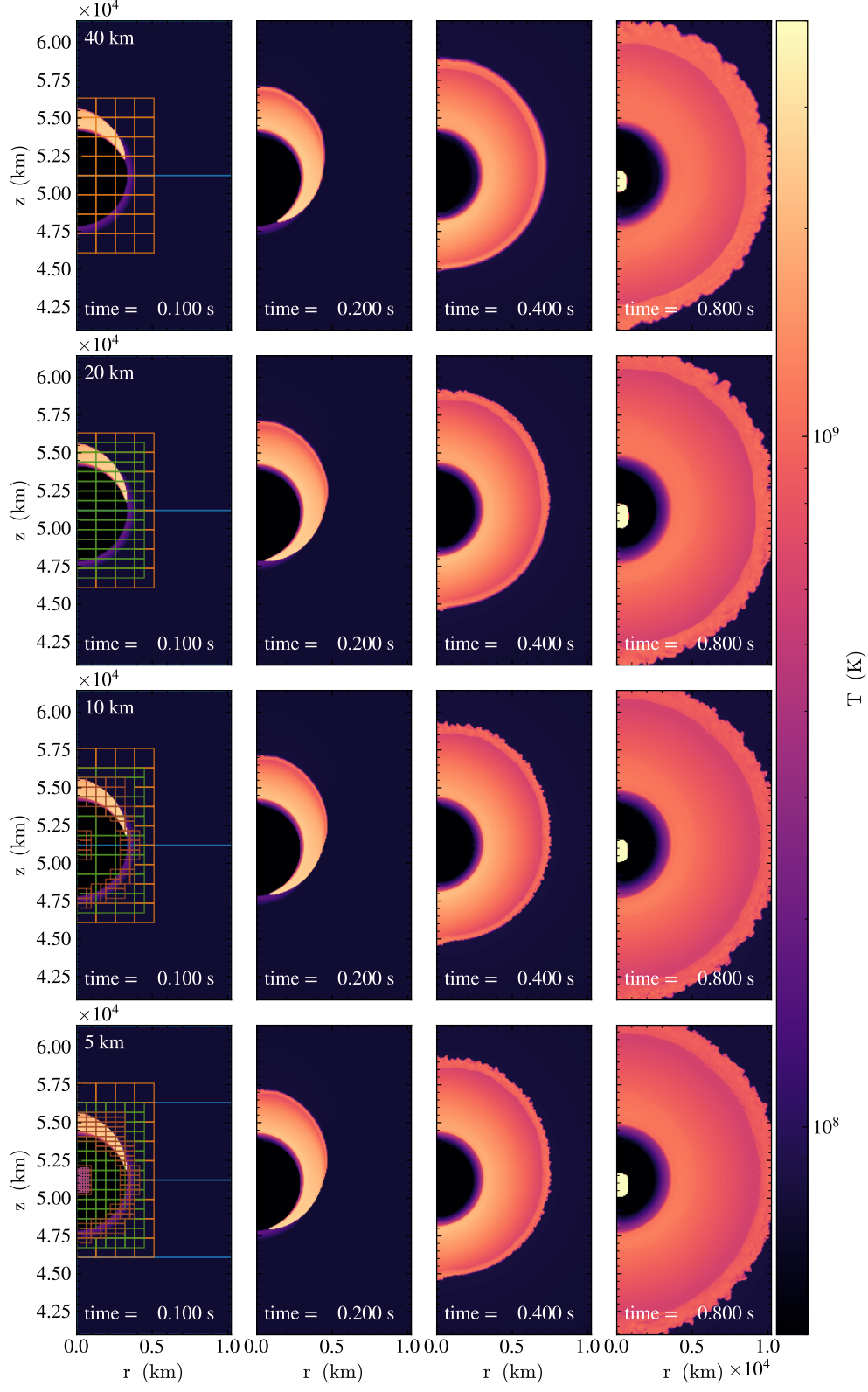
### 3.3. Spatial resolution

Figure 8 shows a time sequence of the simplified-SDC simulation with  $\text{CFL} = 0.2$  and our standard tolerances ( $\epsilon_{\text{abs}} = \epsilon_{\text{rel}} = 10^{-5}$ ) at 4 different maximum spatial resolutions: 40 km, 20 km, 10 km, and 5 km (these are SDC-40km, our original SDC-0.2 simulation, SDC-10km, and SDC-5km in Table 1). For the SDC-40km run, we simply use one fewer level of refinement compared to our SDC-0.2 simulation. For the SDC-10km run, we add an additional level of refinement (another jump of  $2\times$ , giving 3 refinement levels total) that captures only the high temperature regions (including the initial He layer) but with the very center always refined by adding an additional refinement tagging criteria on densities  $\rho > 7.5 \times 10^7 \text{ g cm}^{-3}$ . For the 5 km run, we add a fourth level of refinement (again a jump of  $2\times$ ), but only allow the refinement at the center to go up to this finest level of refinement. The idea is to understand the effect of increased resolution on the C detonation ignition. We confirmed that for the SDC-5km simulation, the C detonation ignited in the region of the domain refined to 5 km. The first column of the figure shows the initial grid structure—the colors corresponding to each level are the same for the different runs. Recall that the boxes at each level can vary in size, but are a multiple of 32 zones in each dimension, with a maximum of 256 zones in any dimension. For the SDC-10km resolution run, we needed to switch from an analytic approximation to the Jacobian to a numerical difference approximation once the C detonation ignited (just like with SDC-0.4), because the evolution became too challenging for the ODE integrator otherwise.

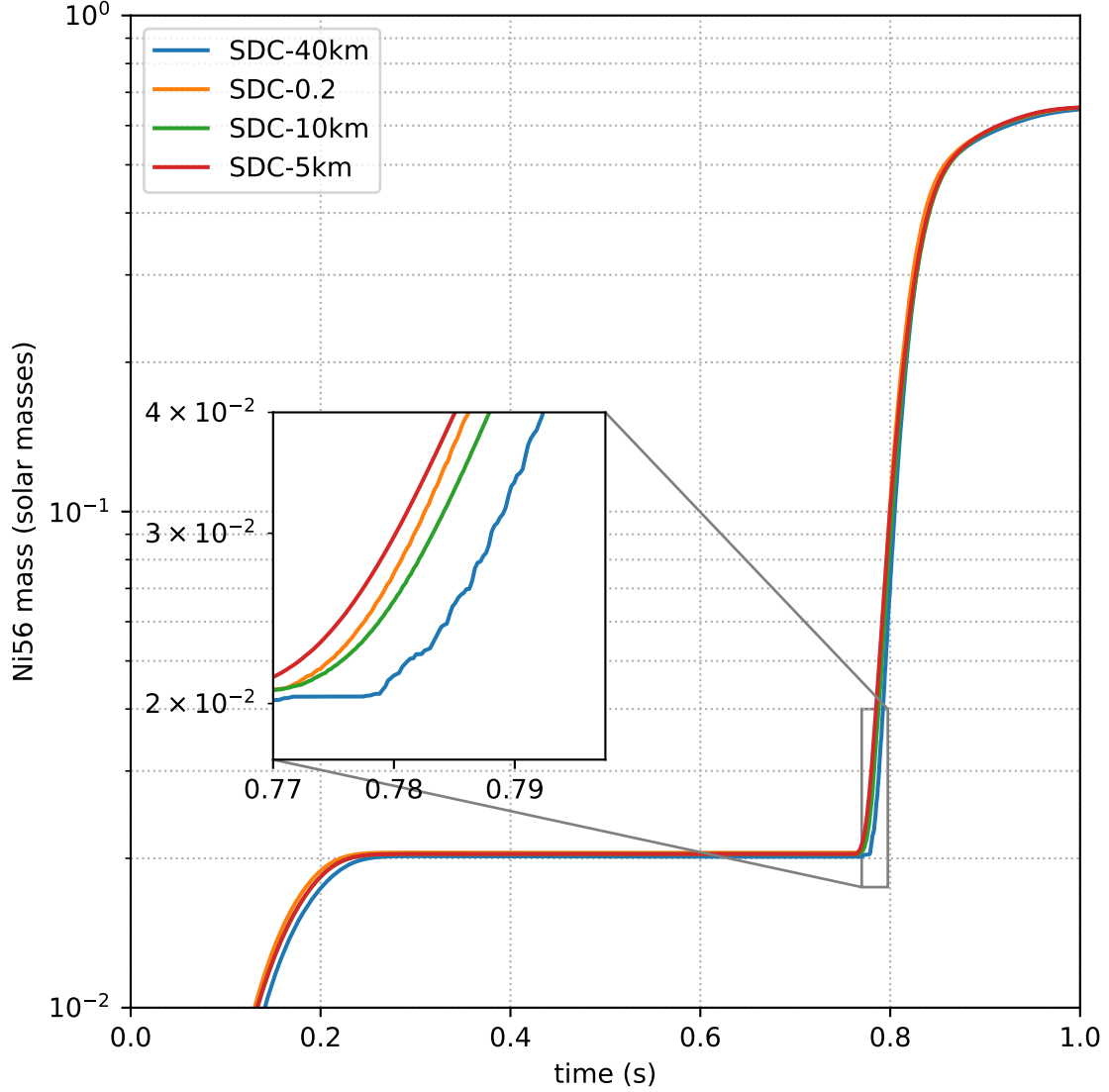
As we see from the time-evolution, the three different resolutions all behave largely the same. The timescale for the He detonation to propagate around the star and the timescale at which the second C detonation ignite match well. Figure 9 shows the  $^{56}\text{Ni}$  mass produced from the three different simulations. Again, the agreement is quite strong.

Figure 10 shows a one-dimensional slice (along the horizontal,  $r$  coordinate) through the detonation at 0.8 s. Both the energy generation rate and temperature are shown. For the energy generation rate, we see both positive and negative regions, indicating that we are attempting to find the NSE state as we evolve. The temperature plot shows that the detonation is very steep, particularly for the highest-resolution simulations. The slightly different detonation positions arise because of the slightly different timings of the He detonation and convergence of the compression wave, which vary with resolution.

We note that these resolution results differ from the conclusions of Rivas et al. (2022). There are a number of reasons why this might be the case. First, the initial models differ—they use a slightly lower mass white dwarf ( $0.98 M_{\odot}$ ). Second, we use a much larger reaction network here that better captures the energetics. This means that the He detonation moves faster in our simulations and the subsequent convergence of the pressure wave will be more on-center, meaning that the ignition of the C detonation occurs at a higher density. Finally, we are using our new simplified-SDC time-



**Figure 8.** Temperature evolution for SDC simulations with CFL=0.2 at 40, 20, and 10 km. For the earliest time in each resolution, the AMR grid structure is shown.



**Figure 9.**  $^{56}\text{Ni}$  mass vs. time for 4 different spatial resolutions, using the simplified-SDC time integration method.

integration, while that work used Strang-splitting. We also have a slightly lower resolution than the finest scale used in [Townesley et al. \(2019\)](#).

#### 4. SUMMARY

Our results suggest that exploring the time-integration method and integrator tolerances are an important part of demonstrating convergence of simulations involving explosive reacting flows in astrophysics. We showed that the simplified-SDC method that we introduced in [Zingale et al. \(2022\)](#) provides an efficient and accurate means to model double detonation Type Ia supernovae. In particular, for converged Ni masses, the simplified-SDC simulations required less computer time than Strang simulations. And for comparable computer time, the simplified-SDC simulations were much more accurate.

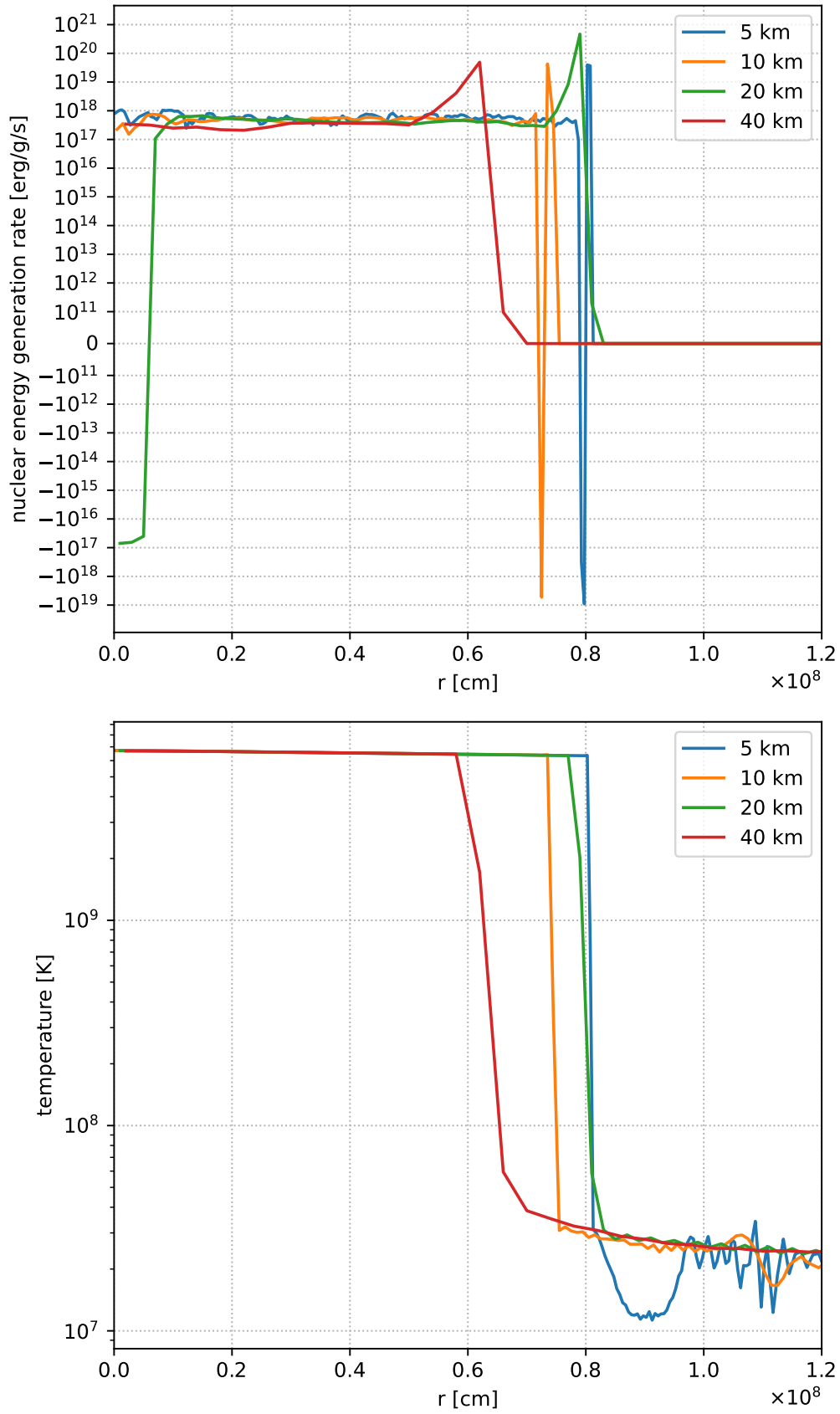


**Figure 10.** Structure of the C detonation at  $t = 0.8$  s for the 3 different resolution runs.

Exploring the integration algorithm and tolerances, in addition to the traditional focus on resolution, was very helpful in understanding convergence. Our suite of simulations show that our nucleosynthesis and dynamics appear to be converged.

The ignition of the carbon detonation remains numerically challenging for the ODE integrator, especially with large timesteps. At the ignition of the C detonation, it is not uncommon for the temperature in a zone during the burn to increase from  $3 \times 10^9$  K to  $6 \times 10^9$  K during a single hydrodynamics timestep. At these temperatures, nuclear statistical equilibrium sets in, and the integrator can spend a lot of time trying to find the equilibrium, reducing its internal timestep in the process. The idea behind simplified-SDC coupling is that the flow should respond to a large amount of energy generated on the grid so the burning is tempered in later iterations, but this may not always be possible over a single timestep. We will explore alternate formulations of energy-based timestep limiters that are compatible with simplified-SDC that might help in this regime. Sometimes, as we saw, the integrator works better in this regime if we use a numerical approximation to the Jacobian. We are exploring heuristics to switch between analytic and numerical Jacobians based on the thermodynamics state as well as auto-differentiation methods for the Jacobian that might work more efficiently. Additionally, we are looking at different classes of ODE integrators that could be more efficient here.

In the near future, we will demonstrate how to include various nuclear statistical equilibrium approximations into the simplified-SDC formalism. [Kushnir & Katz \(2020\)](#) showed how enforcing NSE can help with the efficiency of the integration. For our integration methods, where temperature varies in the reaction network as we integrate, the procedure is more complicated. We can begin a burn with the full network and then need to switch to NSE midway through, once the temperature increases to the point where NSE is established. Care must be taken to do this in a second-order fashion in the simplified-SDC framework.

We will use the simplified-SDC simulation framework demonstrated here to explore the science case of the double detonation SN Ia model. The initial state of the atmosphere is not still, but there will be a convective velocity field built up to the ignition of the detonation. This has been modeled ([Jacobs et al. 2016](#); [Glasner et al. 2018](#)) and we can explore how the detonation propagation is affected by this state. It is straightforward to consider larger networks in our framework, as needed, using `pynucastro`. The follow-on goal is to add more iron-group nuclei and the weak rates that link them to our current network and explore the distribution of iron and nickel produced in these explosions.

The main three-dimensional effect to explore is multi-point ignition. This was looked at in [Moll & Woosley \(2013\)](#). The question is whether the ignition of the central detonation still happens when multiple He detonations send compression waves inward. They found that it still can occur, but this should be revisited with larger networks and our new integration methodology. On the OLCF Frontier machine, a 20 km resolution simulation in 3D requires about  $100\times$  more compute time, which translates into  $\mathcal{O}(10^4)$  node hours, spread across 1024 GPUs initially (more will be needed as it refines). This is feasible with our simulation framework.

Castro is open-source and freely available at <https://github.com/AMReX-Astro/Castro>. The problem setup used here is available in the git repo as `subchandra`. The reaction network infrastructure is contained in the AMReX-Astro Microphysics repository at <https://github.com/AMReX-Astro/Microphysics>. The initial model routines are available at [https://github.com/AMReX-Astro/initial\\_models](https://github.com/AMReX-Astro/initial_models).

The work at Stony Brook was supported by DOE/Office of Nuclear Physics grant DE-FG02-87ER40317. This research used resources of the National Energy Research Scientific Computing Center, a DOE Office of Science User Facility supported by the Office of Science of the U. S. Department of Energy under Contract No. DE-AC02-05CH11231. This research was supported by the Exascale Computing Project (17-SC-20-SC), a collaborative effort of the U.S. Department of Energy Office of Science and the National Nuclear Security Administration. This research used resources of the Oak Ridge Leadership Computing Facility at the Oak Ridge National Laboratory, which is supported by the Office of Science of the U.S. Department of Energy under Contract No. DE-AC05-00OR22725, awarded through the DOE INCITE program. We thank NVIDIA Corporation for the donation of a Titan X and Titan V GPU through their academic grant program. This research has made use of NASA’s Astrophysics Data System Bibliographic Services.

*Facilities:* NERSC, OLCF

*Software:* AMReX (Zhang et al. 2019), Castro (Almgren et al. 2010, 2020), GCC (<https://gcc.gnu.org/>), helmeos (Timmes & Swesty 2000), linux (<https://www.kernel.org/>), matplotlib (Hunter 2007, <http://matplotlib.org/>), NetworkX (Hagberg et al. 2008), NumPy (Oliphant 2007; van der Walt et al. 2011), pynucastro (E. Willcox & Zingale 2018; Smith et al. 2023), python (<https://www.python.org/>), SymPy (Meurer et al. 2017), valgrind (Nethercote & Seward 2007), VODE (Brown et al. 1989), yt (Turk et al. 2010)

## REFERENCES

- Alastuey, A., & Jancovici, B. 1978, ApJ, 226, 1034, doi: [10.1086/156681](https://doi.org/10.1086/156681)
- Almgren, A., Sazo, M. B., Bell, J., et al. 2020, Journal of Open Source Software, 5, 2513, doi: [10.21105/joss.02513](https://doi.org/10.21105/joss.02513)
- Almgren, A. S., Beckner, V. E., Bell, J. B., et al. 2010, ApJ, 715, 1221, doi: [10.1088/0004-637x/715/2/1221](https://doi.org/10.1088/0004-637x/715/2/1221)
- AMReX-Astro initial\_models team, Boyd, B., Smith Clark, A., Willcox, D., & Zingale, M. 2023, AMReX-Astro/initial\_models: Release 23.09, 23.09, Zenodo, doi: [10.5281/zenodo.8305501](https://doi.org/10.5281/zenodo.8305501)
- AMReX-Astro Microphysics Development Team, Bishop, A., Fields, C. E., et al. 2023, AMReX-Astro/Microphysics: Release 23.08, 23.08, Zenodo, doi: [10.5281/zenodo.8206742](https://doi.org/10.5281/zenodo.8206742)
- Boos, S. J., Townsley, D. M., Shen, K. J., Caldwell, S., & Miles, B. J. 2021, ApJ, 919, 126, doi: [10.3847/1538-4357/ac07a2](https://doi.org/10.3847/1538-4357/ac07a2)
- Bourlioux, A., Layton, A. T., & Minion, M. L. 2003, Journal of Computational Physics, 189, 651
- Brown, P. N., Byrne, G. D., & Hindmarsh, A. C. 1989, SIAM J. Sci. and Stat. Comput., 10, 1038, doi: [10.1137/0910062](https://doi.org/10.1137/0910062)
- Bryan, G. L., Norman, M. L., Stone, J. M., Cen, R., & Ostriker, J. P. 1995, Comput. Phys. Commun., 89, 149, doi: [10.1016/0010-4655\(94\)00191-4](https://doi.org/10.1016/0010-4655(94)00191-4)
- Chen, Z., Zingale, M., & Eiden, K. 2023
- Colella, P. 1990, J. Comput. Phys., 87, 171, doi: [10.1016/0021-9991\(90\)90233-q](https://doi.org/10.1016/0021-9991(90)90233-q)
- Colella, P., & Glaz, H. M. 1985, J. Comput. Phys., 59, 264, doi: [10.1016/0021-9991\(85\)90146-9](https://doi.org/10.1016/0021-9991(85)90146-9)



- Colella, P., & Woodward, P. R. 1984, *J. Comput. Phys.*, 54, 174, doi: [10.1016/0021-9991\(84\)90143-8](https://doi.org/10.1016/0021-9991(84)90143-8)
- Cyburt, R. H., Amthor, A. M., Ferguson, R., et al. 2010, *ApJS*, 189, 240, doi: [10.1088/0067-0049/189/1/240](https://doi.org/10.1088/0067-0049/189/1/240)
- Dutt, A., Greengard, L., & Rokhlin, V. 2000, *BIT Numerical Mathematics*, 40, 241, doi: [10.1023/A:102233890](https://doi.org/10.1023/A:102233890)
- E. Willcox, D., & Zingale, M. 2018, *JOSS*, 3, 588, doi: [10.21105/joss.00588](https://doi.org/10.21105/joss.00588)
- Eiden, K., Zingale, M., Harpole, A., et al. 2020, *ApJ*, 894, 6, doi: [10.3847/1538-4357/ab80bc](https://doi.org/10.3847/1538-4357/ab80bc)
- Fink, M., Hillebrandt, W., & Röpke, F. K. 2007, *A&A*, 476, 1133, doi: [10.1051/0004-6361:20078438](https://doi.org/10.1051/0004-6361:20078438)
- Fryxell, B., Olson, K., Ricker, P., et al. 2000, 131, 273–334
- Fryxell, B. A., Müller, E., & Arnett, D. 1989, *MPA Preprint* 449
- Glasner, S. A., Livne, E., Steinberg, E., Yalinewich, A., & Truran, J. W. 2018, *MNRAS*, 476, 2238, doi: [10.1093/mnras/sty421](https://doi.org/10.1093/mnras/sty421)
- Graboske, H. C., Dewitt, H. E., Grossman, A. S., & Cooper, M. S. 1973, *ApJ*, 181, 457, doi: [10.1086/152062](https://doi.org/10.1086/152062)
- Gronow, S., Collins, C., Ohlmann, S. T., et al. 2020, *A&A*, 635, A169, doi: [10.1051/0004-6361/201936494](https://doi.org/10.1051/0004-6361/201936494)
- Gronow, S., Collins, C. E., Sim, S. A., & Röpke, F. K. 2021, *A&A*, 649, A155, doi: [10.1051/0004-6361/202039954](https://doi.org/10.1051/0004-6361/202039954)
- Hagberg, A. A., Schult, D. A., & Swart, P. J. 2008, in *Proceedings of the 7th Python in Science Conference*, ed. G. Varoquaux, T. Vaught, & J. Millman, Pasadena, CA USA, 11 – 15
- Hunter, J. D. 2007, *Comput. Sci. Eng.*, 9, 90, doi: [10.1109/mcse.2007.55](https://doi.org/10.1109/mcse.2007.55)
- Itoh, N., Totsuji, H., Ichimaru, S., & Dewitt, H. E. 1979, *ApJ*, 234, 1079, doi: [10.1086/157590](https://doi.org/10.1086/157590)
- Jacobs, A. M., Zingale, M., Nonaka, A., Almgren, A. S., & Bell, J. B. 2016, *ApJ*, 827, 84, doi: [10.3847/0004-637X/827/1/84](https://doi.org/10.3847/0004-637X/827/1/84)
- Katz, M. P., Zingale, M., Calder, A. C., et al. 2016, *ApJ*, 819, 94, doi: [10.3847/0004-637x/819/2/94](https://doi.org/10.3847/0004-637x/819/2/94)
- Katz, M. P., Almgren, A., Sazo, M. B., et al. 2020, in *Proceedings of the International Conference for High Performance Computing, Networking, Storage and Analysis, SC '20* (IEEE Press). <https://dl.acm.org/doi/abs/10.5555/3433701.3433822>
- Kushnir, D., & Katz, B. 2020, *MNRAS*, 493, 5413, doi: [10.1093/mnras/staa594](https://doi.org/10.1093/mnras/staa594)
- Kushnir, D., Katz, B., Dong, S., Livne, E., & Fernández, R. 2013, *ApJL*, 778, L37, doi: [10.1088/2041-8205/778/2/L37](https://doi.org/10.1088/2041-8205/778/2/L37)
- Ma, H., Woosley, S. E., Malone, C. M., Almgren, A., & Bell, J. 2013, *ApJ*, 771, 58, doi: [10.1088/0004-637X/771/1/58](https://doi.org/10.1088/0004-637X/771/1/58)
- Meurer, A., Smith, C. P., Paprocki, M., et al. 2017, *PeerJ Comput. Sci.*, 3, e103, doi: [10.7717/peerj-cs.103](https://doi.org/10.7717/peerj-cs.103)
- Miller, G., & Colella, P. 2002, *J. Comput. Phys.*, 183, 26, doi: [10.1006/jcph.2002.7158](https://doi.org/10.1006/jcph.2002.7158)
- Moll, R., & Woosley, S. E. 2013, *ApJ*, 774, 137, doi: [10.1088/0004-637X/774/2/137](https://doi.org/10.1088/0004-637X/774/2/137)
- Nethercote, N., & Seward, J. 2007, in *Proceedings of the 2007 ACM SIGPLAN conference on Programming language design and implementation - PLDI '07*, PLDI '07 (New York, NY, USA: ACM Press), 89–100, doi: [10.1145/1250734.1250746](https://doi.org/10.1145/1250734.1250746)
- Nomoto, K. 1982, *ApJ*, 253, 798, doi: [10.1086/159682](https://doi.org/10.1086/159682)
- Oliphant, T. E. 2007, *Comput. Sci. Eng.*, 9, 10, doi: [10.1109/mcse.2007.58](https://doi.org/10.1109/mcse.2007.58)
- Pakmor, R., Edelmann, P., Röpke, F. K., & Hillebrandt, W. 2012, *MNRAS*, 424, 2222, doi: [10.1111/j.1365-2966.2012.21383.x](https://doi.org/10.1111/j.1365-2966.2012.21383.x)
- Papatheodore, T. L., & Messer, O. E. B. 2014, *ApJ*, 782, 12, doi: [10.1088/0004-637X/782/1/12](https://doi.org/10.1088/0004-637X/782/1/12)
- Polin, A., Nugent, P., & Kasen, D. 2019, *ApJ*, 873, 84, doi: [10.3847/1538-4357/aafb6a](https://doi.org/10.3847/1538-4357/aafb6a)
- Radhakrishnan, K., & Hindmarsh, A. C. 1993, *Lawrence Livermore National Laboratory Report UCRL-ID-113855*, 124
- Rivas, F., Harris, J. A., Hix, W. R., & Messer, O. E. B. 2022, *arXiv e-prints*, arXiv:2205.12370. <https://arxiv.org/abs/2205.12370>
- Roy, N. C., Tiwari, V., Bobrick, A., et al. 2022, *ApJL*, 932, L24, doi: [10.3847/2041-8213/ac75e7](https://doi.org/10.3847/2041-8213/ac75e7)
- Shen, K. J., & Bildsten, L. 2009, *ApJ*, 699, 1365, doi: [10.1088/0004-637X/699/2/1365](https://doi.org/10.1088/0004-637X/699/2/1365)
- . 2014, *ApJ*, 785, 61, doi: [10.1088/0004-637X/785/1/61](https://doi.org/10.1088/0004-637X/785/1/61)

- Shen, K. J., Kasen, D., Miles, B. J., & Townsley, D. M. 2018, *ApJ*, 854, 52, doi: [10.3847/1538-4357/aaa8de](https://doi.org/10.3847/1538-4357/aaa8de)
- Smith, A. I., Johnson, E. T., Chen, Z., et al. 2023, *The Astrophysical Journal*, 947, 65, doi: [10.3847/1538-4357/acbaff](https://doi.org/10.3847/1538-4357/acbaff)
- Strang, G. 1968, *SIAM J. Numer. Anal.*, 5, 506, doi: [10.1137/0705041](https://doi.org/10.1137/0705041)
- Svakhine, N., Jang, Y., Ebert, D., & Gaither, K. 2005, in *VIS 05. IEEE Visualization*, 2005., 687–694, doi: [10.1109/VISUAL.2005.1532858](https://doi.org/10.1109/VISUAL.2005.1532858)
- Taubenberger, S. 2017, in *Handbook of Supernovae*, ed. A. W. Alsabti & P. Murdin, 317, doi: [10.1007/978-3-319-21846-5\\_37](https://doi.org/10.1007/978-3-319-21846-5_37)
- Timmes, F. X., & Swesty, F. D. 2000, *ASTROPHYS J SUPPL S*, 126, 501, doi: [10.1086/313304](https://doi.org/10.1086/313304)
- Townsley, D. M., Miles, B. J., Shen, K. J., & Kasen, D. 2019, *ApJL*, 878, L38, doi: [10.3847/2041-8213/ab27cd](https://doi.org/10.3847/2041-8213/ab27cd)
- Townsley, D. M., Miles, B. J., Timmes, F. X., Calder, A. C., & Brown, E. F. 2016, *ApJS*, 225, 3, doi: [10.3847/0067-0049/225/1/3](https://doi.org/10.3847/0067-0049/225/1/3)
- Turk, M. J., Smith, B. D., Oishi, J. S., et al. 2010, *ApJS*, 192, 9, doi: [10.1088/0067-0049/192/1/9](https://doi.org/10.1088/0067-0049/192/1/9)
- van der Walt, S., Colbert, S. C., & Varoquaux, G. 2011, *Comput. Sci. Eng.*, 13, 22, doi: [10.1109/mcse.2011.37](https://doi.org/10.1109/mcse.2011.37)
- Wallace, R. K., Woosley, S. E., & Weaver, T. A. 1982, *ApJ*, 258, 696, doi: [10.1086/160119](https://doi.org/10.1086/160119)
- Woosley, S. E., & Weaver, T. A. 1984, in *American Institute of Physics Conference Series*, Vol. 115, *AIP Conference Proceedings*, ed. S. E. Woosley (AIP), 273–+, doi: [10.1063/1.34531](https://doi.org/10.1063/1.34531)
- Zhang, W., Almgren, A., Beckner, V., et al. 2019, *JOSS*, 4, 1370, doi: [10.21105/joss.01370](https://doi.org/10.21105/joss.01370)
- Zingale, M., Chen, Z., Rasmussen, M., et al. 2023, *Metadata for Sensitivity of Simulations of Double Detonation Type Ia Supernova to Integration Methodology*, Zenodo, doi: [10.5281/zenodo.8287512](https://doi.org/10.5281/zenodo.8287512)
- Zingale, M., Katz, M. P., Nonaka, A., & Rasmussen, M. 2022, *The Astrophysical Journal*, 936, 6, doi: [10.3847/1538-4357/ac8478](https://doi.org/10.3847/1538-4357/ac8478)
- Zingale, M., Katz, M. P., Willcox, D. E., & Harpole, A. 2021, *Research Notes of the AAS*, 5, 71, doi: [10.3847/2515-5172/abf3cb](https://doi.org/10.3847/2515-5172/abf3cb)
- Zingale, M., Nonaka, A., Almgren, A. S., et al. 2013, *ApJ*, 764, 97, doi: [10.1088/0004-637x/764/1/97](https://doi.org/10.1088/0004-637x/764/1/97)